






Article

Nanometric Cu-ZnO Particles Supported on N-Doped Graphitic Carbon as Catalysts for the Selective CO₂ Hydrogenation to Methanol

Lu Peng¹, Bogdan Jurca² , Alberto Garcia-Baldovi¹, Liang Tian¹ , German Sastre¹ , Ana Primo¹, Vasile Parvulescu^{2,*}, Amarajothi Dhakshinamoorthy³  and Hermenegildo Garcia^{1,*} 

¹ Instituto de Tecnología Química, Consejo Superior de Investigaciones Científicas-Universitat Politècnica de Valencia, Av. De los Naranjos s/n, 46022 Valencia, Spain; lu.peng@mpikg.mpg.de (L.P.); baldovi.alber@gmail.com (A.G.-B.); ltian@itq.upv.es (L.T.); gsastre@itq.upv.es (G.S.)

² Department of Organic Chemistry, Biochemistry and Catalysis, University of Bucharest, B-dul Regina Elisabeta 4-12, 030016 Bucharest, Romania; bjurca@gw-chimie.math.unibuc.ro

³ Departamento de Química, Universitat Politècnica de València, C/Camino de Vera, s/n, 46022 Valencia, Spain; admguru@gmail.com

* Correspondence: vasile.parvulescu@chimie.unibuc.ro (V.P.); hgarcia@qim.upv.es (H.G.)

Abstract: The quest for efficient catalysts based on abundant elements that can promote the selective CO₂ hydrogenation to green methanol still continues. Most of the reported catalysts are based on Cu/ZnO supported in inorganic oxides, with not much progress with respect to the benchmark Cu/ZnO/Al₂O₃ catalyst. The use of carbon supports for Cu/ZnO particles is much less explored in spite of the favorable strong metal support interaction that these doped carbons can establish. This manuscript reports the preparation of a series of Cu-ZnO@(N)C samples consisting of Cu/ZnO particles embedded within a N-doped graphitic carbon with a wide range of Cu/Zn atomic ratio. The preparation procedure relies on the transformation of chitosan, a biomass waste, into N-doped graphitic carbon by pyrolysis, which establishes a strong interaction with Cu nanoparticles (NPs) formed simultaneously by Cu²⁺ salt reduction during the graphitization. Zn²⁺ ions are subsequently added to the Cu-graphene material by impregnation. All the Cu/ZnO@(N)C samples promote methanol formation in the CO₂ hydrogenation at temperatures from 200 to 300 °C, with the temperature increasing CO₂ conversion and decreasing methanol selectivity. The best performing Cu-ZnO@(N)C sample achieves at 300 °C a CO₂ conversion of 23% and a methanol selectivity of 21% that is among the highest reported, particularly for a carbon-based support. DFT calculations indicate the role of pyridinic N doping atoms stabilizing the Cu/ZnO NPs and supporting the formate pathway as the most likely reaction mechanism.

Keywords: heterogeneous catalysis; CO₂ hydrogenation; N-doped graphene; methanol synthesis



Citation: Peng, L.; Jurca, B.; Garcia-Baldovi, A.; Tian, L.; Sastre, G.; Primo, A.; Parvulescu, V.; Dhakshinamoorthy, A.; Garcia, H. Nanometric Cu-ZnO Particles Supported on N-Doped Graphitic Carbon as Catalysts for the Selective CO₂ Hydrogenation to Methanol. *Nanomaterials* **2024**, *14*, 476. <https://doi.org/10.3390/nano14050476>

Academic Editors: Nikolaos Dimitratos and Francesc Viñes Solana

Received: 18 January 2024

Revised: 28 February 2024

Accepted: 29 February 2024

Published: 6 March 2024



Copyright: © 2024 by the authors. Licensee MDPI, Basel, Switzerland. This article is an open access article distributed under the terms and conditions of the Creative Commons Attribution (CC BY) license (<https://creativecommons.org/licenses/by/4.0/>).

1. Introduction

Methanol is among the most valuable products that can derive hydrogenation from CO₂ [1–3]. Being in the liquid state at ambient conditions, methanol has other important advantages compared to alternative products formed in CO₂ hydrogenation, including water solubility, non-corrosiveness, high volumetric energy content, and easy transformation into gasoline [4,5] and aromatics [6,7], among other chemicals [8,9]. Although methanol is currently produced on a large multi-ton scale, and there was an estimated 100 millions of metric tons produced in 2020, there is still the possibility to considerably increase methanol production [10], particularly if application of methanol as a fuel or hydrogen carrier is finally implemented [11–13]. In any case, market forecasts indicate that methanol production will at least double by 2030 [12].

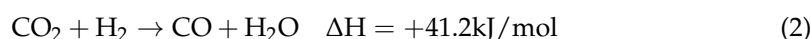
Since formic acid has a low H₂ content and is corrosive, another important advantage of methanol vs. formic acid is its much higher mass and volumetric energy content,

about four times higher than that of formic acid [14,15]. Methanol can be used directly as transportation fuel in combustion engines [15] and it can also be directly used as liquid fuel in proton exchange membrane fuel cells [16]. Methanol is also considered a liquid organic hydrogen carrier [17,18], with a H₂ storage capacity of about 19 wt.% [18,19]. Although methanol reforming will still emit unwanted CO₂, the cycle could have a zero CO₂ footprint if methanol is in turn formed from CO₂ [20]. Equation (1) corresponds to methanol synthesis from CO₂ hydrogenation.



As indicated in Equation (1), the partial CO₂ hydrogenation to methanol is an exothermic reaction, with the equilibrium towards methanol formation being more favorable at low temperatures and high pressures [21,22]. However, the slow reaction kinetics determine that in order to achieve measurable reaction rates, heating of the system and the use of suitable catalysts are required to form methanol.

At high temperatures, CO₂ conversion can be limited by equilibrium composition. In addition, besides methanol, CO appears generally as a competing product (Equation (2)). Typical CO₂ hydrogenation mixtures are composed of methanol and CO in various proportions accompanied by lesser amounts of methane, thus decreasing methanol selectivity. Formation of CO and CH₄ prevails in CO₂ hydrogenation at high temperatures.



Due to these constraints, CO₂ hydrogenation to methanol is carried out at temperatures in a range from 250 to 300 °C and high pressures, for which a compromise between thermodynamics and kinetics requirements can be reached. Also, to overcome this thermodynamic limitation, photocatalytic CO₂ reduction to methanol is gaining importance, including the use of g-C₃N₄ [22–24].

After the discovery by BASF of copper chromite (Cu-CrO₃) as a catalyst for CO₂ hydrogenation to methanol [25], the most widely used catalyst is copper and zinc oxide supported on alumina (Cu-ZnO/Al₂O₃), which is considered as the current benchmark catalyst for the process [25]. The typical atomic Cu/Zn proportion is 2:1 and loading on Al₂O₃ can be over 30 wt.% [26–30]. Although the catalyst is generally denoted as Cu-ZnO, in situ studies suggest that Cu-ZnO is a precursor of the active species formed under the reaction conditions by Cu restructuring, ZnO chemical reduction to Zn metal, and Cu-Zn alloying [31,32]. Thus, even though under ambient conditions Zn is present as oxide and Cu and Zn are in different phases, the as-prepared Cu-ZnO/Al₂O₃ should be considered a precursor of the active sites that have been proposed to be Cu NPs decorated by Zn atoms [32]. Besides alumina, zirconia in different crystallographic phases is considered also as a suitable support [33–35].

In spite of the fact that Cu-ZnO/Al₂O₃ was reported many years ago and considering the current intense research on catalytic CO₂ hydrogenation to methanol [23,33,36], progress in the development of alternative, more efficient, catalysts that could promote methanol synthesis from CO₂ at lower temperatures is still unsatisfactory [33] or based on less abundant elements [37–39]. Among the non-containing-Cu catalysts, indium oxide can promote CO₂ hydrogenation to methanol with a high selectivity [37–39]. Besides facets of In₂O₃, oxygen vacancies are the active sites [40]. Pd doping increases the activity of In₂O₃ without much negative influence on the selectivity [41]. However, indium is considered as a scarce element, particularly compared with abundant Cu and Zn, and it is included in the list of critical raw materials to be avoided [42].

In a series of articles, we have been showing that N-doped graphitic carbons are suitable supports to develop highly selective Fe-Co catalysts for various CO₂ hydrogenation reactions, including the Sabatier reaction [43], the reverse water gas shift (RWGS) (Equation (2)) [44], and for the formation of C₂₊ products [45]. In this context, it is also of interest to expand the use of N-doped graphitic carbon matrices as supports for Cu-ZnO

NPs [Cu-ZnO@(N)C] and to determine their catalytic activity for methanol synthesis under operation conditions compatible with the thermodynamic limitations of the process. In this way, the materials here prepared based on chitosan derived from biomass wastes represent a clear example of waste valorization, applying circular economy principles. The transformation of chitosan into a N-doped graphitic carbon, supporting metal NPs to be used as catalysts, considerably increases the value of the biomass waste.

In comparison to inorganic oxides, carbonaceous supports for Cu-ZnO have been significantly less studied, with most of these studies being limited to carbon nanotubes for methanol synthesis from CO/H₂ [46] and steam reforming of methanol [47]. In one of the few precedents on the use of carbon supports, Cu-CuO and ZnO were formed in a porous carbon FDU-15 obtained by pyrolysis of resol, observing a similar performance for CO₂ hydrogenation to methanol than the benchmark BASF catalyst [48]. Therefore, the catalytic activity of Cu-ZnO@(N)C samples still appears to be worth exploring. As it will be shown below, the experimental data support that Cu-ZnO@(N)C is an efficient, selective, and stable catalyst for partial CO₂ hydrogenation to methanol, resulting in a notable methanol productivity of 83 g_{CH₃OH} kg_{catalyst}⁻¹ h⁻¹.

2. Materials and Methods

2.1. Synthesis of Samples Cu@(N)C and Cu-ZnO@(N)C

Cu@(N)C (sample 1) and Cu-ZnO@(N)C (samples 2–6) were obtained by dissolving 1 g chitosan with 625 µL acetic acid in 50 mL Milli-Q water. After chitosan dissolved completely, the solution was introduced dropwise, with a syringe (0.8 mm diameter needle), in an aqueous solution of sodium hydroxide (500 mL, 2 M). The hydrogel microspheres were formed immediately and immersed in NaOH solution for 2 h and then profusely washed with distilled water to pH 7. Afterwards, the resulting hydrogel microspheres were washed by a series of ethanol/water baths with an increasing concentration of ethanol (10, 30, 50, 70, 90, 100 vol.%, respectively) for 15 min in each and immersed in 100 mL Cu(OAc)₂-ethanol solution with different concentrations, as indicated in Table S1, for 2 days with a slow stirring, then washed with anhydrous ethanol, and subsequently dried by supercritical CO₂. Drying using supercritical CO₂ ensures high porosity and large surface area of the aerogel microspheres in comparison with alternative drying procedures [44]. The resulting aerogel microspheres were pyrolyzed under Ar flow (200 mL/min), increasing the temperature at a rate of 2 °C/min up to 200 °C for 2 h and then to 900 °C for 2 h. The as-prepared samples did not exhibit pyrophoric properties. The resulting Cu@(N)C was ground into powder and immersed in 30 mL Zn(OAc)₂-ethanol solution with different concentrations for 2 days with slow stirring. After removal of ethanol at 60 °C overnight, the Zn²⁺-containing Cu@(N)C was heated at a rate of 2 °C/min up to 200 °C for 2 h to obtain the final Cu-ZnO@(N)C.

2.2. Preparation of Cu-ZnO/Al₂O₃

Copper and zinc oxide supported on alumina (Cu-Zn/Al₂O₃) were prepared by impregnation method in two or one steps. Al₂O₃ powder (270 mg) was dispersed into an ethanol solution (20 mL) of Cu(OAc)₂ (254.5 mg) and the suspension was stirred at room temperature overnight until the solvent evaporated. Then, the obtained powder was pyrolyzed under Ar flow (200 mL/min), increasing the temperature at a rate of 2 °C/min up to 200 °C for 2 h and then to 900 °C for 2 h. After cooling at room temperature, the resulting Cu/Al₂O₃ powder was impregnated in ethanol solution (20 mL) with Zn(OAc)₂ (10 mg) and the suspension was stirred at room temperature overnight until the solvent evaporated. The resulting powder was annealed at a rate of 2 °C/min up to 200 °C for 2 h under Ar flow (200 mL/min). Another analogous Cu-Zn/Al₂O₃ sample in which Cu-impregnated Al₂O₃ was not submitted to pyrolysis was also prepared (Cu-Zn/Al₂O₃-wp, wp meaning without pyrolysis). A third sample was prepared as Cu-Zn/Al₂O₃.wp except that the impregnation of Cu(OAc)₂ and Zn(OAc)₂ was carried out with the same amounts and times but in a single step (Cu-Zn/Al₂O₃-imp).

2.3. Sample Characterization

X-ray diffraction (XRD) patterns were obtained in a Philips XPert diffractometer (Košice, Slovakia) (40 kV and 45 mA) equipped with a graphite monochromator employing Ni-filtered Cu K α radiation (1.541178 Å). Raman spectra were collected with a Horiba Jobin Yvon-Labram HR UV-visible-NIR (Kyoto, Japan) (200–1600 nm). Raman microscope spectrometer model had a 514 nm laser. The carbon and nitrogen content of the samples was determined by combustion chemical analysis by using a CHNS FISOONS elemental analyzer (Spain). The chemical analysis was determined by ICP-OES (iCAP 7400, Thermo Scientific, Waltham, MA, USA) from the mother liquor after digesting the Cu-ZnO@(N)C samples in aqua regia at 60 °C for one day. High-resolution field emission scanning electron microscopy (HR-FESEM) images were acquired by using a Zeiss GeminiSEM500 apparatus (Jena, Germany). High-resolution transmission electron microscope (HR-TEM) images were recorded in a JEOL JEM 2100F (Košice, Slovakia) under an accelerating voltage of 200 kV coupled with an X-Max 80 energy-dispersive X-ray detector (Oxford instruments, Abingdon, UK). This HR-TEM is equipped with dark-field and high-angle field image detectors that facilitate the observation of phase contrast with different atomic numbers. Samples for measurement were prepared by dropping a few drops of the suspended material in ethanol or dichloromethane on a carbon-coated nickel grid and drying at room temperature overnight. The average metal particle size was determined by measuring the diameter of a statistically relevant number of metal NPs in dark field TEM images using the program J-image. The results of this measurement are presented in the furthest-right column of Table 1.

Table 1. List of samples under study and their main analytical and physicochemical parameters.

Sample No.	Cu (wt.%) ^a	Zn (wt.%) ^a	Total Cu + Zn (wt.%) ^a	Molar Ratio (Cu/Zn)	C (wt.%) ^b	N (wt.%) ^b	Average Metal Particle Size (nm) ^c
1	7.9	-	7.9	-	77.0	5.4	1.4 ± 0.3
2	4.8	9.4	14.2	0.5	64.7	3.9	1.4 ± 0.4
3	7.7	2.4	10.1	3.2	70.4	7.1	1.2 ± 0.3
4	8.4	2.0	10.4	4.2	72.4	5.1	1.0 ± 0.3
5	8.2	1.6	9.8	5.1	68.4	4.5	1.3 ± 0.2
6	8.7	1.1	9.8	7.9	72.5	5.1	1.0 ± 0.2

^a Determined by ICP-OES analysis after dissolving the metals in aqua regia; ^b it is assumed that the rest to 100% is residual oxygen; ^c determined by DF-HRTEM. Particle size of 7.8 nm was calculated by Scherrer equation for sample 4.

2.4. Computational Models and Methods

Periodic DFT calculations were conducted using the Cambridge Serial Total Energy Package (CASTEP) module with the exchange–correlation functional described by Perdew–Burke–Ernzerhof (revised version for solids) within the generalized gradient approximation (GGA-PBESol). Tkatchenko and Scheffler (TS) dispersion corrections, scheme, were incorporated along with the exchange and correlation functional to improve the structural and vibrational properties. Slabs were separated by 15 Å along [001], perpendicular to the surface. A self-consistent field method (tolerance 1.0×10^{-7} eV/atom) was employed in conjunction with plane-wave basis sets with a cutoff energy of 500 eV in reciprocal space. All structures were geometry optimized until energy was converged to 1.0×10^{-6} eV/atom, maximum force to 0.025 eV/Å, and maximum displacement to 5.0×10^{-3} Å.

The transition states of every elementary reaction in the CO₂ hydrogenation process were obtained by the complete linear synchronous (LST) and quadratic synchronous transit (QST) methods. The adsorption energy of species over the ZnCu/N-C models was calculated as $E_b = E_{\text{total}} - E_A - E_{\text{sur}}$, where E_{total} represents the total energy of the catalytic surface with the adsorbed molecule and E_A and E_{sur} are the energies of isolated adsorbate molecule and the clean surface, respectively. The energy of an isolated molecule

(E_A) is computed by placing it in the same lattice box (about $15 \times 15 \times 18 \text{ \AA}^3$). The activation energy barriers (E_a) of every step of the elementary reactions are defined as $E_a = E_{TS} - E_{IS}$, where E_{IS} and E_{TS} are the total energy of the initial state (IS) and transition state (TS), respectively.

2.5. Catalyst Testing

Samples 1–6 were tested for CO₂ hydrogenation in a PID Eng&Tech setup (Microactivity Spain) equipped with a stainless steel (316 SS) fixed-bed tube microreactor (Autoclave Engineers) featured with an inner K-type thermocouple in contact with the catalyst packed bed. Flow rates of reagent gases (H₂ 5.0-Linde and CO₂ 4.5-Linde) were controlled with two calibrated mass flow controllers (EL-FLOW Select-Bronkhorst, Nijverheidsstraat, The Netherlands). At least two independent catalytic tests were performed for each sample.

For each test, 40 mg of catalyst powder was introduced in the reactor, air was removed by flushing the system at room temperature for 15 min with ten times the flow rates used during the catalytic tests, followed by 10 min at the flow rates used during the experiments ($3.2 \text{ mL}\cdot\text{min}^{-1} \text{ H}_2$, $0.8 \text{ mL}\cdot\text{min}^{-1} \text{ CO}_2$). The reactor was afterwards slowly pressurized at 40 bars without changing the flow rates of the gas reagents. Two successive GC injections were performed with the gases passing through the reactor at room temperature to check the stability of the gas-phase composition inside the pressurized reactor. Four reaction temperatures from 150 to 300 °C with steps of 50 °C were investigated. For each temperature, GC injection was performed 90 min after the stabilization of the temperature to achieve a steady-state regime of the reactor setup.

Gas samples from the reactor output were passed through a transfer line kept thermostated at 110 °C to be analyzed using an Agilent 7890A gas chromatography instrument with TCD detection. Product separation was performed using capillary PLOT columns: molecular sieve (RT-Molsieve 5A-Restek, for CO, CO₂, and light hydrocarbons) and divinylbenzene (SupelQ-Supelco, for methanol) with H₂ carrier gas (linear velocities between 30 and 41 cm/s). Each gas sample was injected through a remote-controlled 6-way valve (A4C6WE-Vici, thermostated at the same temperature as the transfer line), with a 90 µL injection loop. The system is operated under continuous flow and some of the experiments are ran for several tens of hours to ensure that the products formed do not derive from the catalyst.

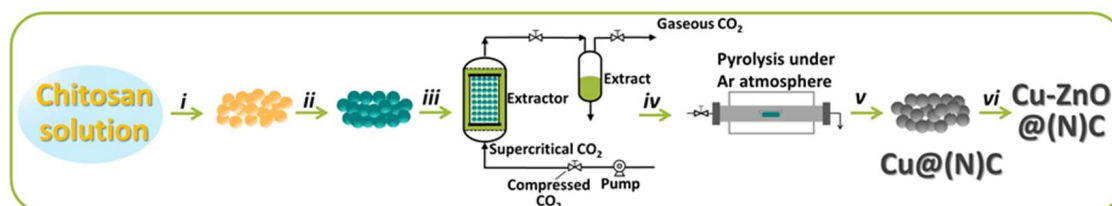
3. Results

3.1. Sample Preparation and Characterization

Initial attempts to prepare Cu-Zn@(N)C were carried out following similar preparation procedures as those described in related precedents on Fe-Co@(N)C [43,44] consisting of the pyrolysis of chitosan powders embedding simultaneously Co and Fe metal ions. During the pyrolysis, chitosan, a polysaccharide of glucosamine, becomes converted in turbostratic N-doped graphitic carbon that can be completely exfoliated to single- or few-layer defective graphene upon sonication [49]. The strong reductive conditions of the hot carbon material during the pyrolysis under inert atmosphere are responsible for the reduction of metal ions to the metallic state [50]. In the present case, chitosan solutions were impregnated with a mixture of Cu(OAc)₂ and Zn(OAc)₂ in various molar ratios. However, due to the low boiling point of Zn metal and the flushing Ar flow, these attempts with Cu-Zn@(N)C were met with failure. Complete Zn evaporation occurred under the conditions of pyrolysis, with only Cu on the (N)C support remaining after pyrolysis.

To overcome this limitation, ZnO was incorporated after the pyrolysis of Cu²⁺ salts adsorbed on chitosan. While it would be possible also to simultaneously incorporate Cu and Zn after chitosan pyrolysis and formation of the N-doped graphitic carbon, it was anticipated that the strong interaction between the Cu metal NPs and the graphene sheets of the carbon resulting from the pyrolysis of Cu²⁺-chitosan [51] would be lost if the sample was prepared by impregnation of N-doped graphitic carbon by Cu(OAc)₂. Data in the literature have shown that pyrolysis at 900 °C of Cu²⁺ ions adsorbed on chitosan renders a material in

which the resulting Cu NPs become strongly grafted on the (N)C support, as deduced from the relatively small particle size, the flat morphology of the Cu NPs, their preferential (111) facet orientation matching the graphene structure, and binding energy shifts in XPS [51–53]. Therefore, in the present study, we proceeded to incorporate $\text{Cu}(\text{OAc})_2$ to the chitosan before pyrolysis to obtain $\text{Cu}@\text{(N)C}$ and, subsequently, to impregnate the desired $\text{Zn}(\text{OAc})_2$ amount on the preformed $\text{Cu}@\text{(N)C}$. It was reasoned that in this way the interaction between the Cu NPs and defective graphene sheets of the carbon matrix as a substrate would be strong [51] and subsequent deposition of $\text{Zn}(\text{OAc})_2$ could still reconstruct the Cu-Zn alloy under the reaction conditions. Scheme 1 illustrates the steps performed in the preparation of $\text{Cu-ZnO}@\text{(N)C}$. Further details can be found in the experimental section.



Scheme 1. Procedure used to prepare the $\text{Cu-ZnO}@\text{(N)C}$ samples under study. (i) Precipitation in NaOH solution of chitosan hydrogel; (ii) water/ethanol exchange and $\text{Cu}(\text{OAc})_2$ impregnation; (iii) supercritical CO_2 drying to remove ethanol; (iv) pyrolysis in Ar atmosphere to obtain $\text{Cu}@\text{(N)C}$; (v) $\text{Zn}(\text{OAc})_2$ impregnation; (vi) thermal treatment.

A series of samples with different atomic Cu/Zn ratios were prepared, trying to cover a wide range of Cu/Zn ratios, including a Cu/Zn ratio of around 3 that is close to the composition of the benchmark $\text{Cu-ZnO}/\text{Al}_2\text{O}_3$ catalyst. Table S1 in the supporting information indicates the exact weights of $\text{Cu}(\text{OAc})_2$ and $\text{Zn}(\text{OAc})_2$ used in the preparation of samples 1–6. Unavoidably, the total Cu + Zn loading on the material varied from sample to sample due to poor control of the weight loss during pyrolysis, although for samples 3–6 the Cu + Zn loading was close to 10%. Note that sample 1 containing only Cu was the material to which $\text{Zn}(\text{OAc})_2$ was not added and, therefore, it has a lower total metal percentage. Table 1 summarizes the set of samples under study, the main Cu-Zn analytical data, and the average metal particle size. It is worth noting that although NaOH was used in the formation of $\text{Cu}(\text{OAc})_2$ -impregnated chitosan beads, due to their water solubility and the sublimation of any possible residual Na during the pyrolysis, the Na content of the final $\text{Cu-ZnO}@\text{(N)G}$ samples was negligible.

The percentages of Cu and Zn in the samples were determined by ICP-OES elemental analysis after treating the $\text{Cu}@\text{(N)C}$ and $\text{Cu-ZnO}@\text{(N)C}$ samples with *aqua regia*, quantifying the metal content of the digested liquor. These data summarized in Table 1 show that the Cu/Zn ratio ranges from ∞ for sample 1, which does not contain ZnO, to 0.53 for sample 2, which is the sample with the highest ZnO proportion. This variation in the Cu/Zn ratio allows one to gain information on the influence of this parameter on methanol selectivity.

High-resolution TEM images show that the $\text{Cu}@\text{(N)C}$ and $\text{Cu-ZnO}@\text{(N)C}$ samples contain metal NPs deposited on 2D defective graphene sheets that constitute the graphitic carbon matrix. Figure 1 shows selected dark-field TEM images taken in three different areas for the samples under study, illustrating that the metal NPs are homogeneously distributed through the carbon matrix as a consequence of the preparation procedure. The white zones of the images indicate where the Cu and Zn metals are present, while the black background indicates the absence of these metals. These images show that the metals are spread out through the carbon matrix. The particle size distribution and the average dimension, ranging from 1.0 ± 0.2 to 1.4 ± 0.4 nm, were determined by measuring the size of a statistically relevant number of those metal NPs. Similar average particle size values for the series of samples are also collected in Table 1, while the corresponding particle size distribution histograms are inserted in the DF-TEM images presented in Figure 1. The absence of large NPs can be observed in the images by the absence of bright dots.

This small dimension of the Cu-ZnO particles in spite of the relatively high loading of metal (up to 14 wt.%) reflects the occurrence of a strong interaction of the Cu NPs with the defective N-doped graphitic carbon that thwarts the growth of the Cu particle even though the pyrolysis is carried out at 900 °C. High-temperature annealing is known to cause agglomeration of small metal NPs, as has been observed in other cases [51]. Thus, the presence of N on the graphitic carbon matrix is a prerequisite to obtain small metal NPs, since in the absence of N doping the resulting particle size is considerably larger, even in the range of 100 nm [54]. There are precedents in the literature claiming the interaction of N atoms on graphene with supported metals, such as Pt resulting in the formation of single atoms or small clusters [55–57].

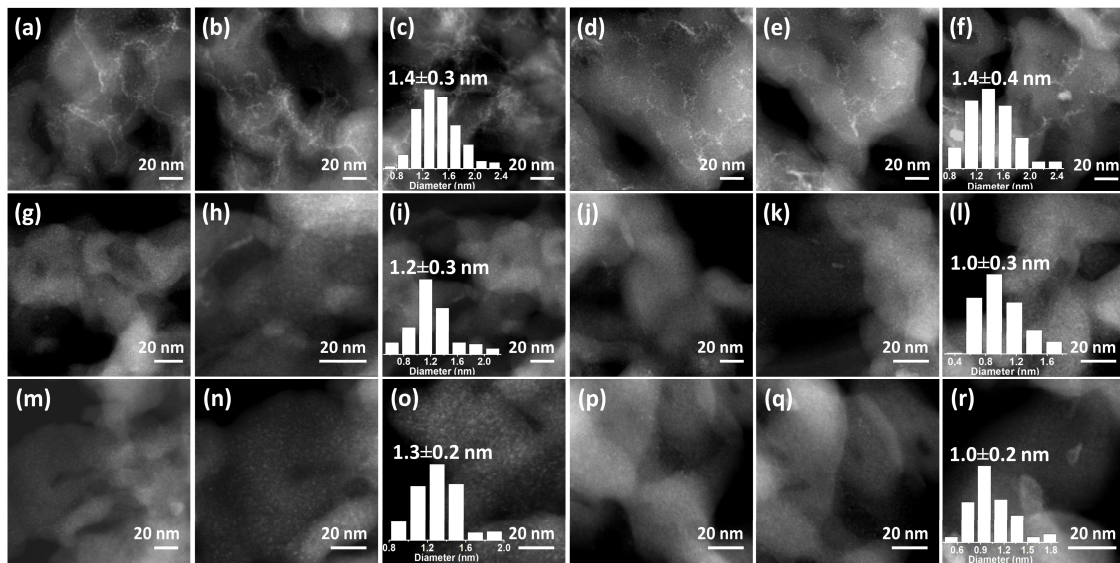


Figure 1. DF-TEM images of samples 1 (a–c), 2 (d–f), 3 (g–i), 4 (j–l), 5 (m–o), and 6 (p–r). Insets: statistical particle size distribution of samples 1–6 according to the main frame image.

Samples 1–6 were also characterized by XRD and Raman spectroscopy (Figure S1). In the XRD patterns, the expected diffraction peaks corresponding to metallic Cu (PDF No. 70-3038) [58] and ZnO (JCPDS No. 36-1451) [59] could be clearly identified for samples 1–6. Figure S1a shows the XRD patterns, indicating the assignment of the peaks, either to Cu metal or ZnO. The relative intensity of the peaks corresponding to ZnO was in accordance with the relative proportion of ZnO in the sample with respect to Cu. In addition, Figure S1 also shows the formation of graphitic carbon with a broad peak appearing around 25° in the XRD pattern. The Scherrer equation was used to quantify the size of Cu and ZnO NPs that are based on the full width at half height of the most intense peaks in XRD resulting in values of 7.8 and 25.0 nm, respectively. These average sizes are much larger than those determined by TEM, appearing in Table 1. This discrepancy could be due to the fact that XRD measures the most crystalline particles in the Cu-ZnO(N)C samples and the small metal particles observed in TEM do not contribute much to the XRD.

The defective nature of N-doped graphene was established by Raman spectroscopy, where the characteristic G and D bands appearing at 1590 and 1350 cm^{-1} , together with resolved overtone 2D at 2700 cm^{-1} , were recorded [60]. Figure S1b plots the representative Raman spectra recorded for each sample 1–6. The relative intensity ratio of the G vs. the D band was about 1.15 and their width at half height is in accordance with values for N-doped graphitic carbons previously reported from chitosan [60].

High-resolution FESEM images at the 100–400 nm scale recorded for the Cu@(N)C and Cu-ZnO@(N)C materials reveal a fluffy, poorly packed, and highly porous morphology of the graphitic carbon matrix acting as a support for the metal-metal oxide NPs. This porous structure is inherited from chitosan aerogel beads dried in super-critical CO_2

in which aggregation of chitosan fibrils by hydrogen bridges has been minimized [61]. Figure 2 and Figure S2 show selected HR-FESEM images for Cu@(N)C (sample 1) and Cu-ZnO@(N)C samples 2–6, illustrating the porous, coral-like structure of the carbonaceous matrix, resulting from the graphitization of the polysaccharide fibrils of the precursor. As expected, no metal NPs could be observed in the HR-FESEM images due to their lower resolution, in agreement with the nanometric particle size of Cu-ZnO NPs measured by HR-TEM.

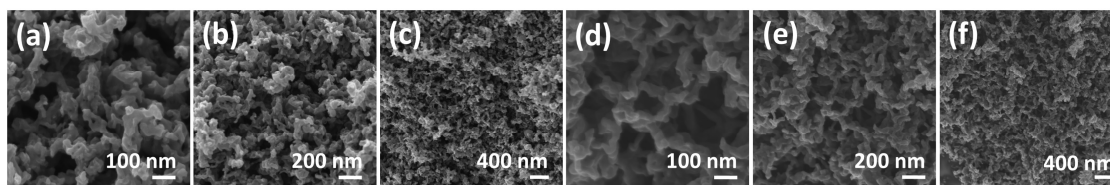


Figure 2. HR-FESEM images of samples 1 (a–c) and 2 (d–f).

To gain information on the interaction between the Cu-ZnO NPs and the (N)G support and to determine the oxidation state of the fresh Cu-ZnO@(N)C samples, XPS analysis of catalyst 4 was performed as a representative sample of the series. XPS analysis of sample 4 revealed the presence of the expected Cu, Zn, C, N, and O elements, but with remarkably different proportions on the surface compared to the analytical data of the bulk material. The elemental proportion based on XPS is provided in Table S2 of the supporting information, while the XPS peaks for the elements and their best deconvolutions are presented in Figure S3. As it can be seen there, the percentages of the Cu and Zn elements on the surface are much below the values expected by the bulk analysis, with C, O, and N of the graphitic carbon being the prevalent surface elements. This result is in accordance with the carbon matrix wrapping the metal NPs. In addition, the surface Cu/Zn XPS ratio is about 0.5, far from the 4.2 ratio measured for the bulk sample. Since samples 2–5 are obtained by Zn impregnation on preformed Cu@(N)C, it appears that the Zn element is more external than the originally introduced Cu metal due to it being incorporated in the samples last. Besides elemental composition, analysis of the high resolution XPS Zn 2p core level peak indicates that it corresponds well to a single ZnO component with a binding energy value of 1022 eV, in accordance with the literature [62]. In contrast, the Cu 2p spectra indicate two components attributable to Cu⁰ and Cu^{II} oxidation states appearing at 932.3 and 934.4 eV, respectively. These values are downshifted by 0.7 eV in the case of Cu⁰ and upshifted by 0.9 eV for Cu^{II}, with respect to the reported literature values for these two oxidation states [63]. These shifts in the binding energy support the occurrence of a strong Cu-(N)G interaction due to the preparation procedure based on high-temperature graphitization, as has been reported earlier [64].

For the sake of comparison and to put into context the catalytic activity of samples 1–6, three samples consisting of Cu-ZnO supported on Al₂O₃ (Cu-ZnO/Al₂O₃) were also prepared. A similar two-step impregnation procedure to that used for the preparation of Cu-ZnO@(N)C was followed for the preparation of Cu-ZnO/Al₂O₃, trying to reproduce the method employed in the preparation of Cu-ZnO@(N)C with Al₂O₃ as a support. A second Cu-ZnO/Al₂O₃-wp (wp meaning without pyrolysis) was also prepared, consecutively adsorbing Cu and Zn, but without submitting the sample to pyrolysis. A third Cu-ZnO/Al₂O₃ was prepared by simultaneous Cu and Zn salts impregnation and subsequent mild baking at 250 °C (Cu-ZnO/Al₂O₃-imp, imp meaning impregnation).

3.2. Catalytic Activity

The objective of the present study is to establish the performance of Cu-ZnO active sites supported on N-doped graphitic carbon as catalysts for the selective partial hydrogenation of CO₂ to methanol, following the lead of previously reported Fe-Co@(N)C catalysts that exhibit very high selectivity for CO₂ hydrogenation to methane [43], CO [44], or C₂₊ [45],

depending on the metal particle size and composition. The use of inorganic supports has been widely studied in the literature [65,66], but there is a limited effort made to gain information about the performance of graphitic carbons as a support in metal catalysts for methanol formation from CO₂ [67].

The catalytic experiments were carried out in a pressurized stainless-steel reactor operating at 40 bar under 4 mL of continuous flow and a H₂ to CO₂ ratio of 4. After considering the known thermodynamic limitations [24], the range of temperatures studied was between 150 and 300 °C in 50 °C steps that were maintained for 1 h before going to the next temperature increase. Systematic calculation of the Weisz–Prater number for each catalyst and conditions indicates that in none of the cases the reaction was under diffusion control (see Table S3 in supporting information). Previous controls operating at 300 °C in the absence of a catalyst showed that the austenite stainless steel reactor converts 1.1% of CO₂ with a selectivity to CO and CH₄ of 92.4 and 7.6%, respectively. This low CO₂ conversion and CO selectivity was maintained with the time of stream in a 3 h test and decreased with the reaction temperature. Table S4 in the supporting information lists the CO₂ conversion and product selectivity of these previous control experiments in the absence of a catalyst at different temperatures. Methanol was undetectable in these control experiments.

Catalyst 1 (Cu@(N)C) containing only Cu did not promote methanol formation and catalyzed mostly the RWGS (Equation (2)), accompanied by some formation of CH₄ and C₂₊ products, with a combined selectivity of about 18%. This relatively high proportion of hydrocarbons in catalyst 1 could indicate the occurrence of some Fischer–Tropsch synthesis in which CO undergoes further hydrogenation of these hydrocarbons.

In contrast to the blank controls and the results with sample 1 lacking ZnO, methanol formation was observed in most of the reactions carried out in the presence of graphitic carbon-supported Cu–ZnO catalysts. The catalytic results achieved by sample 1 make clear that the presence of ZnO is required to drive the selectivity towards methanol. Analysis of the reaction products shows that besides the formation of methanol and CO as the major products, lesser amounts of CH₄, C₂H₆, and C₃H₈ (below a combined percentage of 5%) are also formed (see Tables S5–S12 and Figure S4). It should be commented that although alkali metal ions can be promoters of the catalytic activity of transition metals in CO₂ hydrogenation reactions and we have used NaOH during the preparation of the present Cu–ZnO@(N)G samples, the Na content in these samples is negligible.

To optimize the methanol formation, the performance of Cu–ZnO@(N)C samples was studied at different temperatures from 150 to 300 °C. Figure 3b shows the variation in CO₂ conversion and product selectivity in the case of sample 4, while the results of other samples are presented in Figure S4. As expected, CO₂ conversion increased for all the catalysts upon increasing the temperature in the 150–300 °C range. Methanol selectivity showed the opposite trend, being higher at lower CO₂ conversions and decreasing in favor of CO at higher temperatures. This general behavior agrees with the thermodynamics of the two main competing reactions presented in Equations (1) and (2), with methanol formation being exothermic and RWGS giving CO, being endothermic [24]. At temperatures of 350 °C or higher, CO₂ conversions increase, but methanol selectivity becomes negligible or even methanol formation becomes undetectable. From the dependence of the CO₂ conversion on the temperature (Figure S6 in supporting information), the apparent activation energies (E_a) for CO₂ hydrogenation in the range of temperatures between 150 and 300 °C were obtained for each catalyst of the series (see Figure S4). Except for sample 3, the E_a was in the range of 50 to 43 kJ mol^{−1}, with the lowest value being for sample 4.

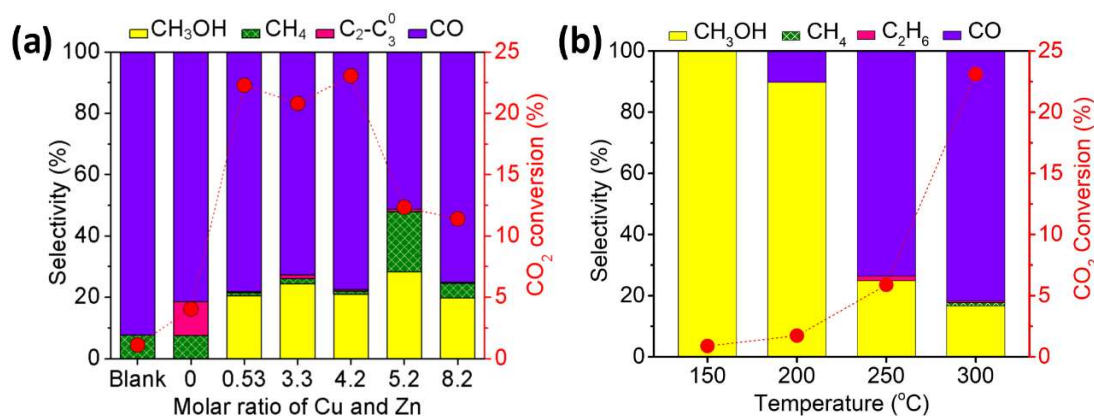


Figure 3. CO₂ conversion and selectivity for samples 1–6 having different molar ratios of Cu and Zn at 300 °C (a) under the same conditions for sample 4 (b) at temperatures from 150 to 300 °C. Reaction conditions: H₂/CO₂ ratio of 4, total flow 4 mL/min, 40 bar, 40 mg catalyst. Blank test: no catalyst.

The series of catalysts using N-doped graphitic carbon as a support did not show a clear influence of the Cu/Zn ratio on methanol selectivity, which was mostly dependent on CO₂ conversion. For the same CO₂ conversion, similar methanol selectivity values were reached regardless of if the Cu/Zn ratio is high (sample 6, Cu/Zn 8.1) or low (sample 2, Cu/Zn 0.53). The main influence of the Cu/Zn ratio appears to be in CO₂ conversion, which was the highest for sample 4, the sample with the lowest E_a. To illustrate differences in the catalytic performance depending on the Cu/Zn ratio, Figure 3a presents the CO₂ conversion and selectivity for samples 1–6 working at 300 °C, 40 bar, at a H₂/CO₂ ratio of 4. As can be seen, besides differences in CO₂ conversion, CO was the main product for all catalysts at 300 °C, although the formation of methanol was observed for all the series of Cu-ZnO@(N)C samples 2–6. Figure S4 provides CO₂ conversion and selectivity for samples 1–6 at 200 and 250 °C. The relative activity order of samples 1–6 found at 300 °C is maintained at 200 and 250 °C, with sample 4 being the best performing catalyst.

From the screening of the Cu-ZnO@(N)C catalysts under study shown in Figure 3a, sample 4 was the best performing catalyst, reaching at 200 °C a conversion of 1.7% with the maximum methanol selectivity of 89.7%. The highest methanol productivity achieved for sample 4 as a catalyst was 2.57 mol_{CH₃OH} kg_{catalyst}⁻¹ h⁻¹ or 82.24 g_{CH₃OH} kg_{catalyst}⁻¹ h⁻¹. To put these data into context, Table S13 in the supporting information provides a comparison of reported data in the literature. Although a comparison of catalyst performance measured under different conditions must be taken always cautiously, Table S13 shows that the methanol productivity achieved in the present study is comparable or overcomes those previously reported for the best catalysts for methanol synthesis from CO₂.

In fact, one key issue that is not reflected in Table S13 is catalyst stability. In the present case, sample 4 exhibits a remarkable catalytic stability, particularly in comparison to the benchmark Cu-ZnO/Al₂O₃. In a long run of 56 h under the reaction conditions, the catalytic activity of sample 4 did not decrease (Figure S7). Furthermore, after this long test at 300 °C, the 56 h used sample 4 exhibit, for two subsequent cycles of increased temperature from 150 to 300 °C in 1 h step of 50 °C temperature increase, identical catalytic data to those measured for the fresh sample presented in Figure S8 and Table S12. These data confirm again the catalyst's stability. This catalyst stability for long reaction runs was also observed for catalysts 2 and 3. It is of note that Cu-ZnO/Al₂O₃-imp did not produce methanol in the range from 200 to 300 °C, with CO and CH₄ being the only products formed (Table S12). Chart S1a,b present chromatograms of the reaction mixture to illustrate the quality of the analysis.

To determine how far from the equilibrium the catalytic values reached for catalysts 2–4, equilibrium data were calculated by minimization of the Gibbs free energy of the system using the RGIBBS module of the Aspenplus© program. For simplicity, these calculations consider the formation of methanol and CO as the only products, ignoring the

small percentage of methane and other hydrocarbons detected in the product mixture in very low proportions (less than 5% according to Tables S2–S11). The composition of the equilibrium mixture was determined in the temperature range between 150 and 300 °C, introducing the operation conditions as the starting composition of the system. The results are presented in Table 2. As it can be seen there, a decrease in the CO₂ conversion from 250 to 350 °C is predicted thermodynamically due to the opposite enthalpy signs of the methanol synthesis (exoergonic, Equation (1)) and the RWGS (endoergonic, Equation (2)). These calculations indicate that the selectivity of methanol 350 °C should be very low. Comparison with the experimental data for catalyst 4 shows that while at 150 and 200 °C, CO₂ conversion is very far from the equilibrium values, the mixture composition approaches the expected equilibrium values in the temperature range from 250 to 300 °C, with theoretical conversions in the range of 25% and methanol selectivity between 60 and 12% under the operation conditions.

Table 2. Calculated equilibrium compositions using Aspenplus as a function of the reaction temperature. Initial conditions: Pressure 40 bar, H₂ 3.2 mL/min, CO₂ 0.8 mL/min.

Temperature (°C)	150	200	250	300	350
CO ₂ conversion (%)	52.1	32.8	24.9	27.5	34.2
Methanol selectivity (%)	99.4	91.6	51.9	12.9	2.6

This catalytic stability of the Cu-ZnO@(N)C samples contrasts with the performance of Cu-ZnO/Al₂O₃, obtained following a two-step impregnation procedure similar to that used for the preparation of Cu-ZnO@(N)C (see experimental section). Cu-ZnO/Al₂O₃ can be taken as a benchmark catalyst with which one can compare the performance of Cu-ZnO@(N)C samples. The catalytic activity of Cu-ZnO/Al₂O₃ is summarized in Table S5. As can be seen there, the CO₂ conversion with the fresh Cu-ZnO/Al₂O₃ samples was somewhat lower than that achieved by the Cu-ZnO@(N)C samples, with a maximum 31% methanol selectivity at 300 °C at 12% CO₂ conversion. Therefore, the performance of the Cu-ZnO@(N)C samples compares well with that of fresh Cu-ZnO/Al₂O₃ (Table S13), with selectivity to methanol decreasing with temperature and CO₂ conversion similarly in both cases. However, it was observed that Cu-ZnO/Al₂O₃ undergoes a notable deactivation with time on stream, becoming severely deactivated in a few tens of hours. After 40 h reaction, the spent Cu-ZnO/Al₂O₃ catalyst is black in color, suggesting coke deposition during the process (see Figure S5 in supporting information). Combustion chemical analysis of a black deactivated Cu-ZnO/Al₂O₃ catalyst showed the presence of over 1% carbon in the material. In the literature, it has been reported that Cu-ZnO/Al₂O₃ undergoes deactivation by sintering of the metal NPs [68] and by coke deposition [69]; not surprisingly, this deactivation happens here for the Cu-ZnO/Al₂O₃ sample in the time scale of tens of hours. Cu-ZnO/Al₂O₃-wp not submitted to pyrolysis behaves similarly, in agreement with the XRD, which shows no difference in the Al₂O₃ crystalline phase due to pyrolysis. Thus, activity and stability data confirm a similar performance and much better stability of Cu-ZnO@(N)C with respect to the Cu-ZnO/Al₂O₃ reference catalyst.

The above results show the advantage of (N)C as a support in comparison to Al₂O₃. To understand the role of (N)C, the type of N atom having a stronger interaction with Cu-ZnO, the CO₂ adsorption of the Cu-Zn cluster, and the plausible reaction mechanism, DFT calculations were carried out.

3.3. Modelling and DFT Calculations

It is well known that the strong metal–support interaction between transition metal clusters and defective carbon (such as N-doped graphene) greatly contributes to the enhancement of the catalytic performance by tuning the electronic structures and improving the stability of, in particular, Cu and Zn-doped Cu clusters [70]. The use of Cu-based catalysts for methanol synthesis via the CO₂ dehydrogenation route is as old as the process

itself and Cu-ZnO/Al₂O₃ catalysts are applicable on an industrial scale in the syngas route [66]. On the other hand, CO₂ hydrogenation to methanol over Cu and Zn-doped Cu clusters supported on graphitic carbon has rarely been reported and its active site is still unclear [71–74].

To better understand the mechanism of methanol synthesis from CO₂, periodic DFT calculations on ZnCu/N-C model catalysts were performed. A 5 × 5 super-cell of graphene with one pyridinic-N and one graphitic-N was built (Figure 4), with the two N-doped atoms being far enough away from each other to make their cross interaction negligible. A Cu cluster with 13 atoms (Cu₁₃) was simulated (Figure 4a), starting from the experimental geometry of these Cu clusters [75].

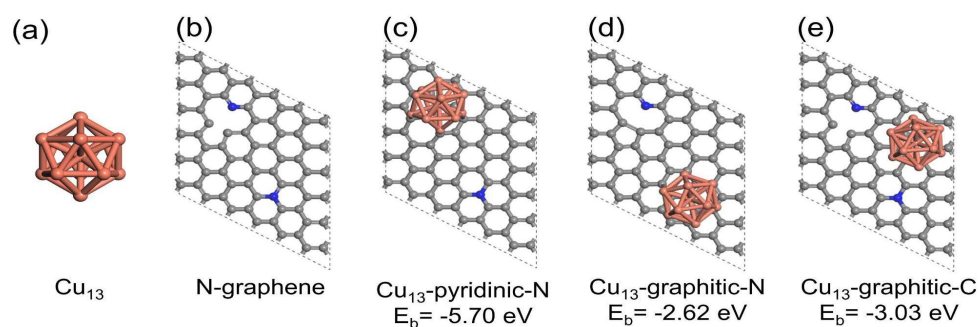


Figure 4. Optimized structural models of: (a) Cu₁₃; (b) N-graphene including two N (blue) defects: pyridinic-N (top-left) and graphitic-N (bottom-right); (c) Cu₁₃ adsorbed on pyridinic-N atom; (d) Cu₁₃ adsorbed on graphitic-N atom; (e) Cu₁₃ adsorbed on graphitic-C atom. Corresponding adsorption energies indicated as E_b for models (c–e). Brown, grey, and blue represent Cu, C, and N atoms, respectively.

The binding strength of Cu₁₃ on different sites of N-doped graphene was first examined by periodic DFT calculations. The binding energies of Cu₁₃ on the pyridinic-N site, graphitic-N site, and graphitic-C site were calculated to be −5.70, −2.62, and −3.03 eV, respectively (Figure 4c–e). The results show that pyridinic N is the most favorable site for anchoring the Cu₁₃ cluster (Figure S9) and the location of Cu₁₃ on this site will be used here onwards. This proposal agrees with the Hirshfeld charge distribution (Table S14), showing a charge transfer from Cu to N-doped graphene of −0.75 e[−], demonstrating that there is a strong interaction between the Cu cluster and N-doped graphene. Apparently, the lone electron pair of pyridinic N interacts strongly with the Cu₁₃ cluster in comparison with graphitic N or C atoms. This strong catalyst–support interaction is believed to provide stability and support to the clusters, preventing their aggregation and maintaining their catalytic activity over multiple reaction cycles.

Additionally to the Cu₁₃ cluster, a Zn-doped Cu cluster (Zn₁Cu₁₂) was also considered. The different substituted sites of the Zn₁Cu₁₂ cluster on pyridinic-N of N-doped graphene were geometry optimized (Figures S10 and S11). Site 12 exhibits the minimum energy, indicating that it is the most stable structure. Thus, we used this model for subsequent calculations on the mechanism of CO₂ hydrogenation to methanol. In this model, the Zn atom is at the core surrounded by the twelve external Cu atoms.

To determine the active site of the reaction, different CO₂ adsorption configurations and sites were computed for the Zn₁Cu₁₂ cluster on the pyridinic-N of N-doped graphene. Figure S12 shows that the line-to-line parallel adsorption has the strongest binding energy. Various non-equivalent line-to-line parallel adsorption sites were subsequently considered for CO₂ adsorption (Figure S13). The results show that one of the Cu-Cu sites (denoted as ‘4-9’, see Figure S13) is the most active for CO₂ adsorption, compared not only among all Cu-Cu sites, but also among N-C, C-C, or Zn-Cu sites (Figure S14). In this absorption mode, two Cu atoms interact simultaneously with the C and the two O atoms of CO₂ that are quasi perpendicularly aligned with the graphene sheet.

Therefore, subsequent intermediates and transition states of CO₂ conversion to methanol were studied on 4-9 Cu-Cu sites for the Zn₁Cu₁₂ cluster on N-doped graphene. Based on reported studies [76,77], two main reaction pathways for CO₂ conversion to methanol were considered in our calculations: the (i) RWGS+CO+hydro pathway: RWGS reaction to produce a CO intermediate followed by its hydrogenation to methanol and (ii) formate pathway: initial hydrogenation of CO₂ to a *HCOO intermediate followed by its hydrogenation and dissociation to methanol. As will be commented below, and in agreement with previous studies [76,77], the present calculations also show the preferred formate pathway on ZnCu/C-N via *HCOOH, *H₂COOH, and *CH₃O intermediates over the RWGS+CO-hydro pathway for methanol synthesis (Figure 5 and Table S15).

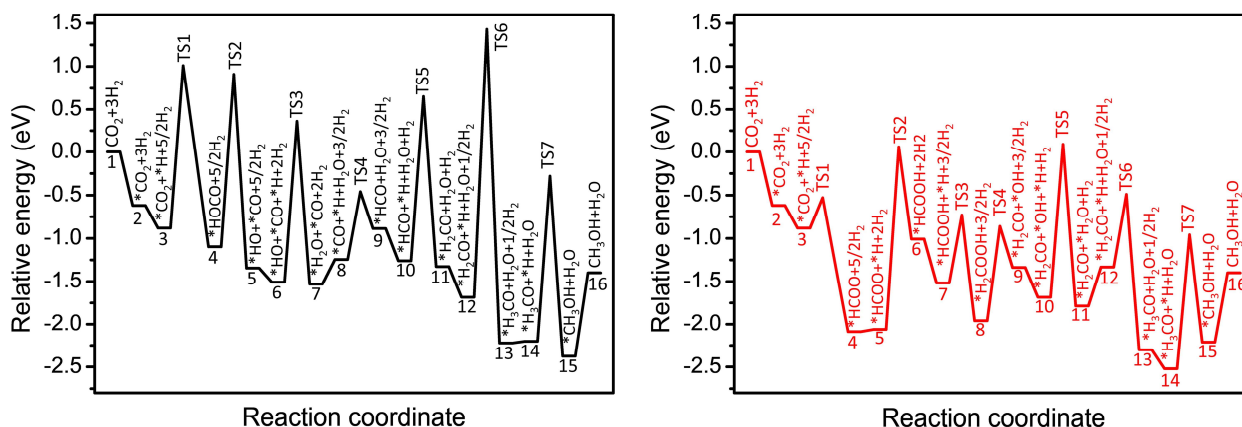


Figure 5. Potential energy diagram for the hydrogenation of CO₂ to CH₃OH. Left: RWGS+CO+hydro pathway. Right: Formate pathway.

3.3.1. Formate Pathway

HCOO* has been considered as the main intermediate for hydrogenating CO₂ to CH₃OH through the formate pathway [65]. Consequently, the rate-determining step is believed to occur in the hydrogenation of HCOO*. Accordingly, our results reveal a low-energy barrier for the formation of HCOO* (0.35 eV, TS1, Figure S15a, Table S15). Then, the rate-determining step is the hydrogenation of *HCOO to form *HCOOH, with an activation energy of 2.12 eV (TS2, Figure S15b, Table S15). Subsequent hydrogenation leads to the formation of *H₂COOH, with an energy barrier of 0.79 eV (TS3, Figure S15c, Table S15). This is followed by the dissociation of *H₂COOH into *H₂CO + *OH, with a barrier of 1.10 eV (TS4, Figure S15d, Table S15), and the hydrogenation of *OH to water, with a barrier of 1.77 eV (TS5, Figure S15e, Table S15). Finally, *H₂CO is hydrogenated twice to form *H₃CO (0.84 eV, TS6, Figure S15f, Table S15) and *CH₃OH (1.56 eV, TS7, Figure S15g, Table S15). These results indicate that the reaction of *HCOO + *H → *HCOOH, with the largest energy barrier (2.12 eV), is the rate-determining step for the synthesis of methanol. Both the low barrier for HCOO* formation and the subsequent largest reaction barrier are lower than the maximum barrier in the RWGS+CO-hydro pathway discussed below, indicating that the formation of methanol should be preferred through the formate pathway.

3.3.2. RWGS+CO+Hydro Pathway

In the RWGS+CO+hydro pathway mechanism, the primary intermediate is CO* instead of HCOO*. Firstly, *CO₂ is hydrogenated to form *HOCO (1.89 eV, TS1, Figure S16a, Table S15). This is followed by the dissociation of *HOCO (TS2, Figure S16b, Table S15) and the hydrogenation of *OH (TS3, Figure S16c, Table S15), with energy barriers of 2.01 and 1.87 eV, respectively. Then, *CO is hydrogenated four times to form *HCO (0.78 eV, TS4, Figure S16d, Table S15), *H₂CO (1.91 eV, TS5, Figure S16e, Table S15), *H₃CO (3.11 eV, TS6, Figure S16f, Table S15), and *CH₃OH (1.92 eV, TS7, Figure S16g, Table S15). CO is expected to be the main product along the RWGS+CO+hydro pathway, since there is a

large energy barrier (3.11 eV, Figure S16 and Table S15) of *H_2CO hydrogenation to *H_3CO (TS6). Since the calculated binding energy of *CO is -1.80 eV, desorption is in competition with subsequent reactions such as TS5 with a barrier of 1.91 eV. This will negatively affect the production of methanol through this pathway.

4. Conclusions

Although Zn metal undergoes evaporation under pyrolysis conditions, it has been possible to prepare a series of Cu-ZnO@(N)G catalysts in two steps in which, first, chitosan embedding Cu(OAc)₂ is pyrolyzed and, subsequently, Zn(OAc)₂ is impregnated and calcined. Since chitosan comes from biomass wastes, the present synthesis represents a clear example of waste valorization and circular economy. The samples show very small metal NPs, about 1 nm average size, well dispersed on the graphitic matrix. These samples act as catalysts for the partial CO₂ hydrogenation to methanol. The formation of significant proportions of CO, accompanied by lesser amounts of methane and higher hydrocarbons, was also observed. Methanol selectivity decreased with CO₂ conversion and reaction temperature in the range of temperatures between 150 and 300 °C, as well as depending on the Cu-ZnO@(N)G catalyst. The presence of ZnO in the catalyst was a prerequisite for methanol formation in (N)C support, but the Cu/Zn atomic ratio influenced CO₂ conversion, rather than methanol selectivity. For the optimal sample, a maximum methanol selectivity of about 89.7% for 1.7% CO₂ conversion and a 25% selectivity at 21% CO₂ conversion and a methanol productivity of 83 g_{CH₃OH} kg_{catalyst}⁻¹ h⁻¹ were reached. These methanol selectivity values are among the highest reported in the literature. DFT calculations indicate that the presence of pyridinic-N atoms on graphene introduces additional active sites and facilitates the adsorption and binding of CuZn clusters, preventing their aggregation and maintaining their catalytic activity over multiple reaction cycles. According to the more favorable formate pathway, the rate-determining step shows an energy barrier of 2.12 eV. This study opens new possibilities for designing and developing efficient catalysts for CO₂ conversion to methanol using N-doped graphene as a substrate.

Supplementary Materials: The following supporting information can be downloaded at: <https://www.mdpi.com/article/10.3390/nano14050476/s1>. References [78–91] are cited in the supplementary materials.

Author Contributions: Conceptualization, A.P., V.P. and H.G.; Computational calculations: L.T. and G.S., Sample preparation: L.P. and A.G.-B.; investigation, B.J.; Writing—review & editing, A.D. All authors have read and agreed to the published version of the manuscript.

Funding: Financial support by the Spanish Ministry of Science and Innovation (CEX-2021-001230-S and PDI2021-0126071-OB-CO21 funded by MCIN/AEI/10.13039/501100011033) and Generalitat Valenciana (Prometeo 2021/038 and Advanced Materials programme Graphica MFA/2022/023 with funding from European Union NextGenerationEU PRTR-C17.I1).

Data Availability Statement: Data are available from the corresponding authors.

Acknowledgments: General ITQ instrumental services area acknowledged for sample analyses and characterization. SGAI-CSIC is acknowledged by the use of computational facilities. A.D. is beneficiary of a grant María Zambrano in Universitat Politècnica de València within the framework of the grants for the retraining in the Spanish university system (Spanish Ministry of Universities, financed by the European Union, NextGeneration EU).

Conflicts of Interest: The authors declare no conflicts of interest.

References

1. Pontzen, F.; Liebner, W.; Gronemann, V.; Rothaemel, M.; Ahlers, B. CO₂-based methanol and DME-Efficient technologies for industrial scale production. *Catal. Today* **2011**, *171*, 242–250. [[CrossRef](#)]
2. Marlin, D.S.; Sarron, E.; Sigurbjörnsson, Ó. Process Advantages of Direct CO₂ to Methanol Synthesis. *Front. Chem.* **2018**, *6*, 446. [[CrossRef](#)] [[PubMed](#)]
3. Choudhury, J. New Strategies for CO₂-to-Methanol Conversion. *ChemCatChem* **2012**, *4*, 609–611. [[CrossRef](#)]

4. Kianfar, E.; Hajimirzaee, S.; Mehr, A.S. Zeolite-based catalysts for methanol to gasoline process: A review. *Microchem. J.* **2020**, *156*, 104822. [[CrossRef](#)]
5. Keil, F.J. Methanol-to-hydrocarbons: Process technology. *Microporous Mesoporous Mater.* **1999**, *29*, 49–66. [[CrossRef](#)]
6. Liu, K.-G.; Bigdeli, F.; Panjehpour, A.; Larimi, A.; Morsali, A.; Dhakshinamoorthy, A.; Garcia, H. Metal organic framework composites for reduction of CO₂. *Coord. Chem. Rev.* **2023**, *493*, 215257. [[CrossRef](#)]
7. Li, T.; Shoinkhorova, T.; Gascon, J.; Ruiz-Martinez, J. Aromatics Production via Methanol-Mediated Transformation Routes. *ACS Catal.* **2021**, *11*, 7780–7819. [[CrossRef](#)]
8. Dalena, F.; Senatore, A.; Marino, A.; Gordano, A.; Basile, M.; Basile, A. Methanol Production and Applications: An Overview. *Methanol* **2018**, *2018*, 3–28.
9. Hutchings, G.J.; Hunter, R. Hydrocarbon formation from methanol and dimethyl ether: A review of the experimental observations concerning the mechanism of formation of the primary products. *Catal. Today* **1990**, *6*, 279–306. [[CrossRef](#)]
10. Dhakshinamoorthy, A.; Navalon, S.; Primo, A.; Garcia, H. Selective Gas-Phase Hydrogenation of CO₂ to Methanol Catalysed by Metal-Organic Frameworks. *Angew. Chem. Int. Ed.* **2024**, *63*, e202311241. [[CrossRef](#)] [[PubMed](#)]
11. Sarp, S.; Hernandez, S.G.; Chen, C.; Sheehan, S.W. Alcohol Production from Carbon Dioxide: Methanol as a Fuel and Chemical Feedstock. *Joule* **2021**, *5*, 59–76. [[CrossRef](#)]
12. Ott, J.; Gronemann, V.; Pontzen, F.; Fiedler, E.; Grossmann, G.; Kersebohm, D.B.; Weiss, G.; Witte, C. *Ullmann's Encyclopedia of Industrial Chemistry*; John Wiley & Sons: Hoboken, NJ, USA, 2000.
13. Garg, N.; Sarkar, A.; Sundararaju, B. Recent developments on methanol as liquid organic hydrogen carrier in transfer hydrogenation reactions. *Coord. Chem. Rev.* **2021**, *433*, 213728. [[CrossRef](#)]
14. Onishi, N.; Laurenczy, G.; Beller, M.; Himeda, Y. Recent progress for reversible homogeneous catalytic hydrogen storage in formic acid and in methanol. *Coord. Chem. Rev.* **2018**, *373*, 317–332. [[CrossRef](#)]
15. Verhelst, S.; Turner, J.W.; Sileghem, L.; Vancoillie, J. Methanol as a fuel for internal combustion engines. *J. Prog. Energy Combust. Sci.* **2019**, *70*, 43–88. [[CrossRef](#)]
16. Wasmus, S.; Küver, A. Methanol oxidation and direct methanol fuel cells: A selective review. *J. Electroanal. Chem.* **1999**, *461*, 14–31. [[CrossRef](#)]
17. Teichmann, D.; Arlt, W.; Wasserscheid, P.; Freymann, R. A future energy supply based on Liquid Organic Hydrogen Carriers (LOHC). *Energy Environ. Sci.* **2011**, *4*, 2767–2773. [[CrossRef](#)]
18. Preuster, P.; Papp, C.; Wasserscheid, P. Liquid Organic Hydrogen Carriers (LOHCs): Toward a Hydrogen-free Hydrogen Economy. *Acc. Chem. Res.* **2017**, *50*, 74–85. [[CrossRef](#)] [[PubMed](#)]
19. Aakko-Saksa, P.T.; Cook, C.; Kiviaho, J.; Repo, T. Liquid organic hydrogen carriers for transportation and storing of renewable energy—Review and discussion. *J. Power Sources* **2018**, *396*, 803–823. [[CrossRef](#)]
20. Milani, D.; Khalilpour, R.; Zahedi, G.; Abbas, A. A model-based analysis of CO₂ utilization in methanol synthesis plant. *J. CO₂ Util.* **2015**, *10*, 12–22. [[CrossRef](#)]
21. Jadhav, S.G.; Vaidya, P.D.; Bhanage, B.M.; Joshi, J.B. Catalytic carbon dioxide hydrogenation to methanol: A review of recent studies. *Chem. Eng. Res. Des.* **2014**, *92*, 2557–2567. [[CrossRef](#)]
22. Kumar, A.; Raizada, P.; Thakur, V.K.; Saini, V.; Khan, A.A.P.; Singh, N.; Singh, P. An overview on polymeric carbon nitride assisted photocatalytic CO₂ reduction: Strategically manoeuvring solar to fuel conversion efficiency. *Chem. Eng. Sci.* **2021**, *230*, 116219. [[CrossRef](#)]
23. Wojtyła, S.; Szmít, K.; Baran, T.J. Type II Heterostructures: The Way Towards Improved Photoelectrochemical Activity of Graphitic Carbon Nitride. *Inorg. Organomet. Polym.* **2018**, *28*, 492–499. [[CrossRef](#)]
24. Xu, X.; Feng, X.; Wang, W.; Song, K.; Ma, D.; Zhou, Y.; Shi, J.-W. Construction of II-type and Z-scheme binding structure in P-doped graphitic carbon nitride loaded with ZnO and ZnTCPP boosting photocatalytic hydrogen evolution. *J. Colloid Interface Sci.* **2023**, *651*, 669–677. [[CrossRef](#)] [[PubMed](#)]
25. Tursunov, O.; Kustov, L.; Kustov, A. A Brief Review of Carbon Dioxide Hydrogenation to Methanol Over Copper and Iron Based Catalysts. *Oil Gas Sci. Technol.-Rev. D'ifp Energ. Nouv.* **2017**, *72*, 30. [[CrossRef](#)]
26. Kamsuwan, T.; Krutpijit, C.; Prasertthdam, S.; Phatanasri, S.; Jongsomjit, B.; Prasertthdam, P. Comparative study on the effect of different copper loading on catalytic behaviors and activity of Cu/ZnO/Al₂O₃ catalysts toward CO and CO₂ hydrogenation. *Heliyon* **2021**, *7*, e07682. [[CrossRef](#)]
27. Pasupulety, N.; Driss, H.; Alhamed, Y.A.; Alzahrani, A.A.; Daous, M.A.; Petrov, L. Studies on Au/Cu–Zn–Al catalyst for methanol synthesis from CO₂. *Appl. Catal. A Gen.* **2015**, *504*, 308–318. [[CrossRef](#)]
28. Xiao, S.; Zhang, Y.; Gao, P.; Zhong, L.; Li, X.; Zhang, Z.; Wang, H.; Wei, W.; Sun, Y. Highly efficient Cu-based catalysts via hydrotalcite-like precursors for CO₂ hydrogenation to methanol. *Catal. Today* **2017**, *281*, 327–336. [[CrossRef](#)]
29. Dasireddy, V.D.; Likozar, B. The role of copper oxidation state in Cu/ZnO/Al₂O₃ catalysts in CO₂ hydrogenation and methanol productivity. *Renew. Energy* **2019**, *140*, 452–460. [[CrossRef](#)]
30. Samimi, F.; Rahimpour, M.R.; Shariati, A. Development of an Efficient Methanol Production Process for Direct CO₂ Hydrogenation over a Cu/ZnO/Al₂O₃ Catalyst. *Catalysts* **2017**, *7*, 332. [[CrossRef](#)]
31. Grunwaldt, J.-D.; Molenbroek, A.; Topsøe, N.-Y.; Topsøe, H.; Clausen, B. In Situ Investigations of Structural Changes in Cu/ZnO Catalysts. *J. Catal.* **2000**, *194*, 452–460. [[CrossRef](#)]

32. Behrens, M.; Studt, F.; Kasatkin, I.; Kühn, S.; Hävecker, M.; Abild-Pedersen, F.; Zander, S.; Girgsdies, F.; Kurr, P.; Knief, B.-L.; et al. The Active Site of Methanol Synthesis over Cu/ZnO/Al₂O₃ Industrial Catalysts. *Science* **2012**, *336*, 893–897. [[CrossRef](#)] [[PubMed](#)]
33. Guil-López, R.; Mota, N.; Llorente, J.; Millán, E.; Pawelec, B.; Fierro, J.L.G.; Navarro, R. Methanol Synthesis from CO₂: A Review of the Latest Developments in Heterogeneous Catalysis. *Materials* **2019**, *12*, 3902. [[CrossRef](#)] [[PubMed](#)]
34. Larmier, K.; Liao, W.C.; Tada, S.; Lam, E.; Verel, R.; Bansode, A.; Urakawa, A.; Comas-Vives, A.; Copéret, C. CO₂-to-Methanol Hydrogenation on Zirconia-Supported Copper Nanoparticles: Reaction Intermediates and the Role of the Metal–Support Interface. *Angew. Chem. Int. Ed.* **2017**, *56*, 2318–2323. [[CrossRef](#)] [[PubMed](#)]
35. Rungtaweivoranit, B.; Baek, J.; Araujo, J.R.; Archanjo, B.S.; Choi, K.M.; Yaghi, O.M.; Somorjai, G.A. Copper Nanocrystals Encapsulated in Zr-based Metal–Organic Frameworks for Highly Selective CO₂ Hydrogenation to Methanol. *Nano Lett.* **2016**, *16*, 7645–7649. [[CrossRef](#)] [[PubMed](#)]
36. Din, I.U.; Shaharun, M.S.; Alotaibi, M.A.; Alharthi, A.I.; Naeem, A. Recent developments on heterogeneous catalytic CO₂ reduction to methanol. *J. CO₂ Util.* **2019**, *34*, 20–33. [[CrossRef](#)]
37. Martin, O.; Martín, A.J.; Mondelli, C.; Mitchell, S.; Segawa, T.F.; Hauert, R.; Drouilly, C.; Curulla-Ferré, D.; Pérez-Ramírez, J. Indium Oxide as a Superior Catalyst for Methanol Synthesis by CO₂ Hydrogenation. *Angew. Chem. Int. Ed.* **2016**, *55*, 6261–6265. [[CrossRef](#)]
38. Chou, C.-Y.; Lobo, R.F. Direct conversion of CO₂ into methanol over promoted indium oxide-based catalysts. *Appl. Catal. A Gen.* **2019**, *583*, 117144. [[CrossRef](#)]
39. Dang, S.; Qin, B.; Yang, Y.; Wang, H.; Cai, J.; Han, Y.; Li, S.; Gao, P.; Sun, Y. Rationally designed indium oxide catalysts for CO₂ hydrogenation to methanol with high activity and selectivity. *Sci. Adv.* **2020**, *6*, eaaz2060. [[CrossRef](#)]
40. Ye, J.; Liu, C.; Mei, D.; Ge, Q. Active Oxygen Vacancy Site for Methanol Synthesis from CO₂ Hydrogenation on In₂O₃(110): A DFT Study. *ACS Catal.* **2013**, *3*, 1296–1306. [[CrossRef](#)]
41. Frei, M.S.; Mondelli, C.; García-Muelas, R.; Kley, K.S.; Puértolas, B.; López, N.; Safonova, O.V.; Stewart, J.A.; Ferré, D.C.; Pérez-Ramírez, J. Atomic-scale engineering of indium oxide promotion by palladium for methanol production via CO₂ hydrogenation. *Nat. Commun.* **2019**, *10*, 3377. [[CrossRef](#)]
42. Navalon, S.; Dhakshinamoorthy, A.; Alvaro, M.; Antonietti, M.; Garcia, H. Active sites on graphene-based materials as metal-free catalysts. *Chem. Soc. Rev.* **2017**, *46*, 4501–4529. [[CrossRef](#)] [[PubMed](#)]
43. Jurca, B.; Peng, L.; Primo, A.; Gordillo, A.; Parvulescu, V.I.; Garcia, H. Co–Fe Nanoparticles Wrapped on N-Doped Graphitic Carbons as Highly Selective CO₂ Methanation Catalysts. *ACS Appl. Mater. Interfaces* **2021**, *13*, 36976–36981. [[CrossRef](#)] [[PubMed](#)]
44. Peng, L.; Jurca, B.; Primo, A.; Gordillo, A.; Parvulescu, V.I.; García, H. Co–Fe Clusters Supported on N-Doped Graphitic Carbon as Highly Selective Catalysts for Reverse Water Gas Shift Reaction. *ACS Sustain. Chem. Eng.* **2021**, *9*, 9264–9272. [[CrossRef](#)]
45. Peng, L.; Jurca, B.; Primo, A.; Gordillo, A.; Parvulescu, V.I.; García, H. High C₂–C₄ selectivity in CO₂ hydrogenation by particle size control of Co–Fe alloy nanoparticles wrapped on N-doped graphitic carbon. *iScience* **2022**, *25*, 104252. [[CrossRef](#)] [[PubMed](#)]
46. Großmann, D.; Dreier, A.; Lehmann, C.; Grünert, W. Methanol synthesis over Cu–ZnO aggregates supported on carbon nanotubes. *Appl. Catal. A Gen.* **2015**, *504*, 351–360. [[CrossRef](#)]
47. Yang, H.-M.; Liao, P.-H. Preparation and activity of Cu/ZnO-CNTs nano-catalyst on steam reforming of methanol. *Appl. Catal. A Gen.* **2007**, *317*, 226–233. [[CrossRef](#)]
48. Duan, H.; Yang, Y.; Singh, R.; Chiang, K.; Wang, S.; Xiao, P.; Patel, J.; Danaci, D.; Burke, N.; Zhai, Y. Mesoporous Carbon-supported Cu/ZnO for Methanol Synthesis from Carbon Dioxide. *Aus. J. Chem.* **2014**, *67*, 907–914. [[CrossRef](#)]
49. Primo, A.; Sánchez, E.; Delgado, J.M.; García, H. High-yield production of N-doped graphitic platelets by aqueous exfoliation of pyrolyzed chitosan. *Carbon* **2014**, *68*, 777–783. [[CrossRef](#)]
50. He, J.; Dhakshinamoorthy, A.; Primo, A.; Garcia, H. Iron Nanoparticles Embedded in Graphitic Carbon Matrix as Heterogeneous Catalysts for the Oxidative C–N Coupling of Aromatic N–H Compounds and Amides. *ChemCatChem* **2017**, *9*, 3003–3012. [[CrossRef](#)]
51. Primo, A.; Esteve-Adell, I.; Blandez, J.F.; Dhakshinamoorthy, A.; Álvaro, M.; Candu, N.; Coman, S.M.; Parvulescu, V.I.; García, H. High catalytic activity of oriented 2.0.0 copper(I) oxide grown on graphene film. *Nat. Commun.* **2015**, *6*, 8561. [[CrossRef](#)]
52. Frindy, S.; El Kadib, A.; Lahcini, M.; Primo, A.; Garcia, H. Isotropic and Oriented Copper Nanoparticles Supported on Graphene as Aniline Guanylation Catalysts. *ACS Catal.* **2016**, *6*, 3863–3869. [[CrossRef](#)]
53. Mateo, D.; Esteve-Adell, I.; Albero, J.; Primo, A.; Garcia, H. Oriented 2.0.0 Cu₂O nanoplatelets supported on few-layers graphene as efficient visible light photocatalyst for overall water splitting. *Appl. Catal. B Environ.* **2017**, *201*, 582–590. [[CrossRef](#)]
54. García-Baldoví, A.; Peng, L.; Santiago-Portillo, A.; Asiri, A.M.; Primo, A.; García, H. Aqueous Phase Methanol Reforming Catalyzed by Fe–Cu Alloy Nanoparticles Wrapped on Nitrogen-Doped Graphene. *ACS Appl. Energy Mater.* **2022**, *5*, 9173–9180. [[CrossRef](#)]
55. Baby, A.; Trovato, L.; Di Valentin, C. Single Atom Catalysts (SAC) trapped in defective and nitrogen-doped graphene supported on metal substrates. *Carbon* **2021**, *174*, 772–788. [[CrossRef](#)]
56. Wu, X.; Feng, B.; Li, W.; Niu, Y.; Yu, Y.; Lu, S.; Zhong, C.; Liu, P.; Tian, Z.; Chen, L. Metal-support interaction boosted electrocatalysis of ultrasmall iridium nanoparticles supported on nitrogen doped graphene for highly efficient water electrolysis in acidic and alkaline media. *Nano Energy* **2019**, *62*, 117–126. [[CrossRef](#)]
57. He, T.; Santiago, A.R.P.; Du, A. Atomically embedded asymmetrical dual-metal dimers on N-doped graphene for ultra-efficient nitrogen reduction reaction. *J. Catal.* **2020**, *388*, 77–83. [[CrossRef](#)]

58. Lin, J.; Zeng, C.; Lin, X.; Xu, C.; Su, C.Y. CNT-Assembled Octahedron Carbon-Encapsulated Cu₃P/Cu Heterostructure by In Situ MOF-Derived Engineering for Superior Lithium Storage: Investigations by Experimental Implementation and First-Principles Calculation. *Adv. Sci.* **2020**, *7*, 2000736. [[CrossRef](#)]
59. Chen, S.-J.; Li, L.-H.; Chen, X.-T.; Xue, Z.; Hong, J.-M.; You, X.-Z. Preparation and characterization of nanocrystalline zinc oxide by a novel solvothermal oxidation route. *J. Cryst. Grow.* **2003**, *252*, 184–189. [[CrossRef](#)]
60. He, J.; Anouar, A.; Primo, A.; García, H. Quality Improvement of Few-Layers Defective Graphene from Biomass and Application for H₂ Generation. *Nanomaterials* **2019**, *9*, 895. [[CrossRef](#)]
61. Taberero, A.; Baldino, L.; Misol, A.; Cardea, S.; Del Valle, E.M.M. Role of rheological properties on physical chitosan aerogels obtained by supercritical drying. *Carbohydr. Polym.* **2020**, *233*, 115850. [[CrossRef](#)]
62. Mar, L.G.; Timbrell, P.Y.; Lamb, R.N. An XPS study of zinc oxide thin film growth on copper using zinc acetate as a precursor. *Thin Solid Films* **1993**, *223*, 341–347. [[CrossRef](#)]
63. Biesinger, M.C. Advanced analysis of copper X-ray photoelectron spectra. *Surf. Interface Anal.* **2017**, *49*, 1325–1334. [[CrossRef](#)]
64. Garcia-Baldovi, A.; Peng, L.; Dhakshinamoorthy, A.; Asiri, A.M.; Primo, A.; García, H. Positive influence of minute Pt addition on the activity of Ni supported on defective graphene for hydrogenation/dehydrogenation of N-ethylcarbazole as liquid organic carrier. *Catal. Commun.* **2023**, *177*, 106641. [[CrossRef](#)]
65. Jiang, X.; Nie, X.; Guo, X.; Song, C.; Chen, J.G. Recent Advances in Carbon Dioxide Hydrogenation to Methanol via Heterogeneous Catalysis. *Chem. Rev.* **2020**, *120*, 7984–8034. [[CrossRef](#)] [[PubMed](#)]
66. Etim, U.J.; Song, Y.; Zhong, Z. Improving the Cu/ZnO-Based Catalysts for Carbon Dioxide Hydrogenation to Methanol, and the Use of Methanol As a Renewable Energy Storage Media. *Front. Energy Res.* **2020**, *8*, 545431. [[CrossRef](#)]
67. Deerattrakul, V.; Dittanet, P.; Sawangphruk, M.; Kongkachuichay, P. CO₂ hydrogenation to methanol using Cu-Zn catalyst supported on reduced graphene oxide nanosheets. *J. CO₂ Util.* **2016**, *16*, 104–113. [[CrossRef](#)]
68. Sun, J.T.; Metcalfe, I.S.; Sahibzada, M. Deactivation of Cu/ZnO/Al₂O₃ Methanol Synthesis Catalyst by Sintering. *Ind. Eng. Chem. Res.* **1999**, *38*, 3868–7382. [[CrossRef](#)]
69. Ren, S.; Fan, X.; Shang, Z.; Shoemaker, W.R.; Ma, L.; Wu, T.; Li, S.; Klinghoffer, N.B.; Yu, M.; Liang, X. Enhanced catalytic performance of Zr modified CuO/ZnO/Al₂O₃ catalyst for methanol and DME synthesis via CO₂ hydrogenation. *J. CO₂ Util.* **2020**, *36*, 82–95. [[CrossRef](#)]
70. Yang, J.; Li, W.; Wang, D.; Li, Y. Electronic Metal-Support Interaction of Single-Atom Catalysts and Applications in Electrocatalysis. *Adv. Mater.* **2020**, *32*, 2003300. [[CrossRef](#)]
71. Fan, Y.J.; Wu, S.F. A graphene-supported copper-based catalyst for the hydrogenation of carbon dioxide to form methanol. *J. CO₂ Util.* **2016**, *16*, 150–156. [[CrossRef](#)]
72. Witoon, T.; Numpilai, T.; Phongamwong, T.; Donphai, W.; Boonyuen, C.; Warakulwit, C.; Chareonpanich, M.; Limtrakul, J. Enhanced activity, selectivity and stability of a CuO-ZnO-ZrO₂ catalyst by adding graphene oxide for CO₂ hydrogenation to methanol. *Chem. Eng. J.* **2018**, *334*, 1781–1791. [[CrossRef](#)]
73. Sun, Y.; Chen, L.; Bao, Y.; Wang, G.; Zhang, Y.; Fu, M.; Wu, J.; Ye, D. Roles of nitrogen species on nitrogen-doped CNTs supported Cu-ZrO₂ system for carbon dioxide hydrogenation to methanol. *Catal. Today* **2018**, *307*, 212–223. [[CrossRef](#)]
74. Deerattrakul, V.; Chukchuan, A.; Thepphankulngarm, N.; Pornjaturawit, J.; Vacharameteevoranun, N.; Chaisuwan, T.; Kongkachuichay, P. Carbon dioxide hydrogenation to methanol over polybenzoxazine-based mesocarbon supported Cu-Zn catalyst. *New J. Chem.* **2021**, *45*, 8283–8290. [[CrossRef](#)]
75. Hu, Q.; Han, Z.; Wang, X.; Li, G.; Wang, Z.; Huang, X.; Yang, H.; Ren, X.; Zhang, Q.; Liu, J. Facile Synthesis of Sub-Nanometric Copper Clusters by Double Confinement Enables Selective Reduction of Carbon Dioxide to Methane. *Angew. Chem. Int. Ed.* **2020**, *59*, 19054–19059. [[CrossRef](#)] [[PubMed](#)]
76. Kattel, S.; Ramírez, P.J.; Chen, J.G.; Rodriguez, J.A.; Liu, P. Active sites for CO₂ hydrogenation to methanol on Cu/ZnO catalysts. *Science* **2017**, *355*, 1296–1299. [[CrossRef](#)] [[PubMed](#)]
77. Wang, Y.; Kattel, S.; Gao, W.; Li, K.; Liu, P.; Chen, J.G.; Wang, H. Exploring the ternary interactions in Cu-ZnO-ZrO₂ catalysts for efficient CO₂ hydrogenation to methanol. *Nat. Commun.* **2019**, *10*, 1166. [[CrossRef](#)] [[PubMed](#)]
78. Segall, M.; Lindan, P.J.; Probert, M.A.; Pickard, C.J.; Hasnip, P.J.; Clark, S.; Payne, M. First-principles simulation: Ideas, illustrations and the CASTEP code. *J. Phys. Condens. Matter* **2002**, *14*, 2717. [[CrossRef](#)]
79. Perdew, J.P.; Ruzsinszky, A.; Csonka, G.I.; Vydrov, O.A.; Scuseria, G.E.; Constantin, L.A.; Zhou, X.; Burke, K. Restoring the density-gradient expansion for exchange in solids and surfaces. *Phys. Rev. Lett.* **2008**, *100*, 136406. [[CrossRef](#)] [[PubMed](#)]
80. Tkatchenko, A.; Scheffler, M. Accurate molecular van der Waals interactions from ground-state electron density and free-atom reference data. *Phys. Rev. Lett.* **2009**, *102*, 073005. [[CrossRef](#)] [[PubMed](#)]
81. Halgren, T.A.; Lipscomb, W.N. The synchronous-transit method for determining reaction pathways and locating molecular transition states. *Chem. Phys. Lett.* **1977**, *49*, 225–232. [[CrossRef](#)]
82. Primo, A.; He, J.; Jurca, B.; Cojocaru, B.; Bucur, C.; Parvulescu, V.I.; Garcia, H. CO₂ methanation catalyzed by oriented MoS₂ nanoplatelets supported on few layers graphene. *Appl. Catal. B Environ.* **2019**, *245*, 351–359. [[CrossRef](#)]
83. Fogler, H. Diffusion and reaction. In *Elements of Chemical Reaction Engineering*; Pearson: Upper Saddle River, NJ, USA, 2006; pp. 813–852.
84. Vannice, M.A.; Joyce, W.H. *Kinetics of Catalytic Reactions*; Springer: Berlin/Heidelberg, Germany, 2005.

85. Hirschfelder, J.O.; Curtiss, C.F.; Bird, R.B. Molecular theory of gases and liquids. In *Molecular Theory of Gases and Liquids*; Wiley: Hoboken, NJ, USA, 1964.
86. Zhu, J.; Su, Y.; Chai, J.; Muravev, V.; Kosinov, N.; Hensen, E.J. Mechanism and nature of active sites for methanol synthesis from CO/CO₂ on Cu/CeO₂. *ACS Catal.* **2020**, *10*, 11532–11544. [[CrossRef](#)]
87. Temvuttirojn, C.; Poo-Arporn, Y.; Chanlek, N.; Cheng, C.K.; Chong, C.C.; Limtrakul, J.; Witoon, T. Role of calcination temperatures of ZrO₂ support on methanol synthesis from CO₂ hydrogenation at high reaction temperatures over ZnO x/ZrO₂ catalysts. *Ind. Eng. Chem. Res.* **2020**, *59*, 5525–5535. [[CrossRef](#)]
88. Oshima, K.; Honma, Y.; Kinoshita, K.; Gao, Z.; Honma, T.; Tada, S.; Satokawa, S. Mechanochemical effect in mixing sponge copper with amorphous ZrO₂ creates effective active sites for methanol synthesis by CO₂ hydrogenation. *J. Phys. Chem. C* **2021**, *125*, 8155–8162. [[CrossRef](#)]
89. Ghosh, S.; Sebastian, J.; Olsson, L.; Creaser, D. Experimental and kinetic modeling studies of methanol synthesis from CO₂ hydrogenation using In₂O₃ catalyst. *Chem. Eng. J.* **2021**, *416*, 129120. [[CrossRef](#)]
90. Chen, S.; Zhang, J.; Song, F.; Zhang, Q.; Yang, G.; Zhang, M.; Wang, X.; Xie, H.; Tan, Y. Induced high selectivity methanol formation during CO₂ hydrogenation over a CuBr₂-modified CuZnZr catalyst. *J. Catal.* **2020**, *389*, 47–59. [[CrossRef](#)]
91. Mureddu, M.; Lai, S.; Atzori, L.; Rombi, E.; Ferrara, F.; Pettinau, A.; Cutrufello, M.G. Ex-LDH-based catalysts for CO₂ conversion to methanol and dimethyl ether. *Catalysts* **2021**, *11*, 615. [[CrossRef](#)]

Disclaimer/Publisher's Note: The statements, opinions and data contained in all publications are solely those of the individual author(s) and contributor(s) and not of MDPI and/or the editor(s). MDPI and/or the editor(s) disclaim responsibility for any injury to people or property resulting from any ideas, methods, instructions or products referred to in the content.